On the geometry of demixing: A study of lipid phase separation on curved surfaces

Rinaldin, M.

CHAPTER 6

LIPID BILAYERS OF DESIGNED CURVATURE ON SUBSTRATES OBTAINED *VIA* MICRO-PRINTING AND REPLICA-MOLDING

Membrane curvature is a fundamental part of the cellular machinery. Highly curved compartments are necessary for cellular transport and the function of organelles relies on their specific shape. In cells, membrane curvature can be generated by different mechanisms. For example, nanoscopic curvature can be achieved by lipid or protein sorting and macroscopic curvature by cytoskeletal scaffolding. In protein-free systems in vitro, membrane curvature can be artificially obtained by, for example, membrane micro-manipulation, phase separation, and supported lipid bilayers fabrication. However, until now, these methods allow for studying a restricted range of shapes only. This chapter presents a general and facile method to obtain membranes of tuneable curvature with high precision. By combining three-dimensional printing and replica-molding lithography, we fabricate scaffolds of designed shape and size suitable for lipid coating. We show that the resulting bilayers are homogeneous and fluid. We demonstrate their potential by using them for fluorescence after photobleaching and phase separation experiments on curved surfaces. Our method can be extended to study single particles and protein diffusion and localisation. We anticipate that it will open new possibilities to investigate curvature sensing proteins and, more generally, the role of membrane curvature in biology.

This chapter is based on:

M. Rinaldin, B. ten Haaf, J. Salaris, E. J. Vegter, C. van der Wel, L. Giomi, and D. J. Kraft, Supported lipid bilayers on 3D micro-printed scaffolds and their applications, *in preparation*.

6.1 Introduction

From neurons and red blood cells to cellular compartments such as the endoplasmatic reticulum and mitochondria, membrane curvature can be remodelled according to a cell's needs[128;197]. For example, during cellular trafficking the membrane of one cell changes its shape to expel spherical vesicles and tubes, which are then fused into another cell's membrane.

The many different ways in which the curvature of a cellular membrane can be adjusted have been widely studied[128;197]. They include a change in the lipid composition, the presence of membrane proteins that induce intrinsic curvature, and cytoskeletal scaffolding. In model lipid bilayers, deformations can be obtained in multiple ways: (1) Highly curved tubes can be pulled out of spherical liposomes by micro-pipettes or beads moved by laser traps[7]. (2) Wrinkles and shape changes can be induced in vesicles with electric fields[198]. (3) Multicomponent liposomes undergoing phase separation often form buds and can drastically change both their geometry and topology of the membrane[4]. (4) Confined lipid bilayers can form spherical or tubular protrusions because of adhesion, strain, and osmotic pressure[199]. (5) Proteins, as BAR domains[200], colloidal particles[94], and active elements[201] can be included in the membrane to generate curvature. (6) Vesicles can be set in contact with topographically patterned substrates and locally assume their curvature[18;19]. (7) Finally, curvature can be imposed on supported lipid bilayers (SLBs) by coating with lipids inhomogeneously curved substrates. Solid substrates commonly used are topographically patterned substrates[5] and colloidal particles, see Chapter 2 and 5.

While these methods have all greatly contributed to the understanding of the role of curvature in membranes, they have some limitations. In method (1) and (2), only specific curved shapes can be obtained, namely small tubes with a radius of curvature ranging from tens to hundreds of nm and wrinkles, respectively. In method (3), the shape and the size of the membrane cannot be controlled because of the complex interaction between curvature, elasticity, and phase separation patterns, which was also the subject of this thesis. In method (4), only spherical and tubular deformations can be obtained. In method (5), the curvatures that can be obtained have a nanometre-scale radius and are not stable in time. In methods (6) and (7), curvatures which are stable for days can be achieved. However, limitations in the shape of colloidal particles and topographically patterned substrates that can be achieved with the available fabrication techniques restrict the design of membrane curvature.

To overcome these limitations, we present in this chapter a method to obtain lipid membranes with designed, tunable, constant, and reproducible shape. To do this, we create SLBs on microstructures obtained from micro-printing and replica-molding lithography with PDMS. By using three-dimensional (3D) printing, we can produce molds with any designed shape. We show that the use of PDMS for replica-molding is necessary to obtain a homogeneous and fully fluid bilayer. The SLBs fabricated with this method can be directly used for experiments to test the effect of membrane curvature on many processes. For example, we present here preliminary experiments on fluorescence recovery after photobleaching (FRAP) and liquid-liquid phase separation. This method allows for a limitless *a priori* design of membrane curvature, does not require the use of

harsh chemicals, such as acids for glass etching used in other works[18], and, finally, because of the top-down approach, it allows for curved membranes which are (straightforwardly) reproducible.

6.2 Methods

6.2.1 Reagents. The lipids (Δ9-Cis) 1,2-dioleoyl-*sn*-glycero-3-phosphocholine (DOPC), 1-palmitoyl-2-oleoyl-*sn*-glycero-3-phosphocholine (POPC), porcine brain sphingomyelin (BSM), ovine wool cholesterol (chol), 1,2-dioleoyl-*sn*-glycero-3-phosphoethanolamine-N-[methoxy(polyethylene glycol)-2000] (DOPE-PEG(2000)), and L-α-Phosphatidyl-ethanolamine-N-(DOPE lissamine rhodamine B sulfonyl) were purchased from Avanti Polar Lipids and stored at −20 °C. 4-(2-hydroxyethyl)-1-piperazineethanesulfonic acid (HEPES, ≥99.5 %) and calcium chloride ($CaCl_2$, Calciumchlorid Dihydrat, ≥99 %) were purchased from Carl Roth. Sodium chloride (NaCl, extra pure) was purchased from Acros Organics. Dipotassium phosphate (K_2HPO_4) and propylene glycol monomethyl ether acetate (PGMA, ≥99.5 %) and trichloro(1H,1H,2H,2H-perfluorooctyl)silane (≥97 %) were purchased from Sigma-Aldrich. Magnesium chloride ($MgCl_2$, for analysis) was purchased from Merck. 2-Propanol (≥99.6 %) was purchased from Honeywell. All solutions were prepared with Milli-Q water (Milli-Q Gradient A10). Silcon wafers of (10.0 ± 0.3) cm diameter, 1 Ω cm resistivity, and 525 ± 25µm thickness were purchased from Siegert Wafer. IP-S photoresist was purchased by Nanoscribe GmbH. Polydimethyl siloxane (PDMS) was purchased from Dow Corning.

6.2.2 Microstructures. Microstructures for SLB formation were prepared by PDMS replica-molding from 3D printed molds.

The first fabrication stage consists iof micro-printing of the molds. The 3D structure of the molds was designed using the software Autodesk Inventor (Autodesk) and processed with the program Describe (Nanoscribe GmbH) to obtain a mesh of points suitable for micro-printing. Subsequently, the molds were fabricated by two-photon lithography using a commercial 3D microprinter (Nanoscribe GmbH, Photonics Professional GT). The commercial photoresist (IP-S, Nanoscribe GmbH) was employed as a pre-polymer. The photoresist was polymerised by exposure to a 780 nm laser focused by a 63x objective (NA=1.48, Carl Zeiss) directly in contact with the photoresist. Slice by slice, small volumes (400 µm x 400 µm x 100 µm) were exposed using galvanic mirrors and stitched together by moving a mechanical stage. The laser power used was 30 mW.

The unpolymerised resist was removed in a bath with PGMA for 15 minutes and rinsed with 2-propanol. The fabrication and the cleaning of the molds were performed under yellow light (λ= 577 - 597 nm) to prevent spontaneous polymerisation.

The second stage of preparation consists of the PDMS replica-molding. The molds were silanised with trichloro(1H,1H,2H,2H-perfluorooctyl)silane under vacuum for 2 hours to prevent irreversible sticking of PDMS on the surface. A PDMS pre-polymer mixture was prepared from a 1:10 elastome:crosslinker mixture by weight. It was degassed for 30 minutes under vacuum, poured onto the molds, and further degassed for 2 hours

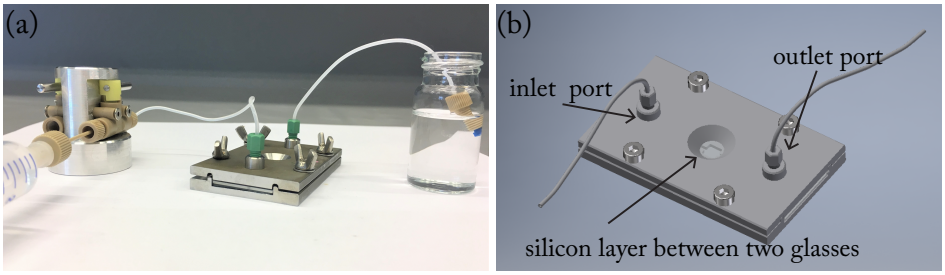

Figure 6.1: The flow cell. (a) Photograph of the assembled flow cell. **(b)** Schematic drawing of the flow cell. The microstructures can be positioned in between the two glasses. The spacing between the glass is set by the thickness of the silicon layer.

to eliminate any bubbles present, which could affect the shape of the microstructures. Then, the microstructures were cured with temperature for 2 hours at 100 °C in an oven to polymerise the PDMS. Finally, the cured structures were peeled from the molds.

Before being used for lipid coating, the microstructures were washed for 10 minutes by sequential sonication in acetone, ethanol, and MilliQ water, following the protocol of Subramaniam *et al.*[5]. The microstructures were then dried in the oven and treated with UV/ozone for one hour to fully hydrophilise the surface. The resulting PDMS microstructures were immediately used for the lipid coating to avoid exponential hydrophobisation of PDMS, which is known to happen after UV/ozone treatment[202].

6.2.3 Lipid coating. SLBs were formed by deposition of small unilamellar vesicles (SUVs) obtained *via* extrusion at high pressure[24]. A mixture of 500 µg of lipids in chloroform (94.8% DOPC, 5% DOPE-PEG(2000), and 0.2% DOPE-Rhodamine, mole ratio) was prepared. The chloroform was evaporated in a vacuum chamber for 2 hours. The lipids were dispersed in HEPES buffer made with 115 mM NaCl, 1.2 mM $CaCl_2$, 1.2 mM $MgCl_2$, 2.4 mM K_2HPO_4, and 20 mM HEPES in 2 gL^{-1} concentration, and allowed to self-assemble in multilamellar vesicles during 30 minutes of vortexing. The solution was extruded 21 times with a mini-extruder (Avanti Polar Lipids) equipped with two 250 µL gas-tight syringes (Hamilton), two drain discs, and one nucleopore track-etch membrane with pores of 0.03 µm diameter (Whatman).

50 µL of SUVs solution diluted in 1 mL of HEPES buffer were slowly flushed into a flow cell containing the PDMS microstructures and incubated for 1 hour. Then, the flow cell was flushed with HEPES buffer to remove excess SUVs.

The flow cell was specifically designed for this experiment and its blueprint was inspired by Brewer and Bianco[203]. The cell can be mechanically assembled, sealed properly, washed, and reused in all its part. We employed it in these experiments for two reasons. First, the geometry of the cell allows for removing the SUVs in excess without putting the sample in contact with air. Second, since the flow cell is completely sealed, it can be used upside-down for imaging. In this way, we could avoid the diffraction of the light through

the PDMS structures and obtain 3D reconstructions of the bilayer. A photograph and schematic drawing of the used flow cell are shown in Figure 6.1.

6.2.4 Sample characterisation and FRAP measurements. The samples were imaged at room temperature with an inverted confocal microscope (Nikon Eclipse Ti-E) equipped with a Nikon A1R confocal scan head with Galvano and resonant scanning mirrors. 20x and 60x air objectives (NA=0.75 and 0.7, respectively) were used. A 561 nm laser was used to excite the Rhodamine dye. The laser was passed through a quarter-wave plate to avoid polarisation of the dyes. The emitted light was separated using a 565-625 nm filter. 3D image stacks were acquired by scanning the sample in the z-direction with a MCL Nano-drive stage and reconstructed with Nikon AR software. During the imaging, the microstructures were positioned upside down in the flow chamber to avoid diffraction effects.

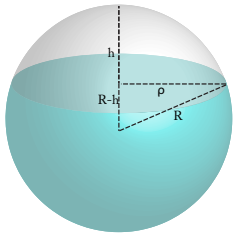

Figure 6.2: Schematic representation of the bleached spherical cap of radius ρ (grey area) on a sphere of radius R.

The fluorescence recovery after photobleaching technique (FRAP) was used to test the mobility of the lipids. A circular area of the fluorescent sample was bleached, the recovery signal was collected, and normalised as:

$$I_{\text{norm}}(t) = \frac{I(t)I_{\text{ref}}(t_0)}{I(t_0)I_{\text{ref}}(t)}, \tag{6.1}$$

where $I_{\text{norm}}(t)$ is the measured intensity $I(t)$ normalised with the initial intensity $I(t_0)$ and corrected for bleaching through measurement of the normalised intensity of a non-bleached reference area $(I_{\text{ref}}(t)/I_{\text{ref}}(t_0))$. The signal was fitted using the following expression:

$$I_{\text{norm}}(t) = A\left(1 - e^{-\frac{t}{\tau_0}}\right), \tag{6.2}$$

where A is the extent of the recovery[204] and τ_0 is related to the half time of recovery by $\tau_{\frac{1}{2}} = \tau_0 \ln(2)$. The diffusion coefficient on flat surfaces was calculated as:

$$D_{FRAP} = \frac{0.22R^2}{\tau_{\frac{1}{2}}}, \tag{6.3}$$

where R is the radius of the bleaching area and 0.22 derives from geometrical arguments, as described by Axerold *et al.*[95]. For FRAP measurements on top of half-spherical structures, Equation 6.3 was modified to take into account that the bleaching area chosen in the experiment was a planar projection of the actual bleached spherical cap (Figure 6.2). For a spherical cap, Equation 6.3 becomes:

$$D_{FRAP} = \frac{4\pi R^2(1 - \sqrt{(1 - \frac{\rho^2}{R^2})})}{\tau_{\frac{1}{2}}}, \tag{6.4}$$

where ρ and R are the bleaching area and half-sphere radius, respectively.

6.3 Results and discussion

6.3.1 SLBs on microstructures fabrication. We fabricated supported lipid bilayers (SLBs) on PDMS substrates made by replica-molding of micro-printed structures. Using this technique, lipid membranes of any top-down designed shape can be obtained. We illustrate in Figure 6.3 the experimental strategy that we developed for fabricating the microstructures (top) and coating them with lipids (bottom). In the following section, we will show that the bilayers that we fabricated are homogenous and mobile and, therefore, they can be used in further experiments to investigate the role of curvature in lipid membranes.

As a first step, we created molds using 3D laser micro-printing, *e.g.* inverted Gaussian bumps (Figure 6.3, top: step 1). Then, we poured a solution of PDMS pre-polymer over the molds (Figure 6.3, top: step 2), which we subsequently cured at a temperature of 100 °C for 2 hours. Finally, we peeled the polymerised PDMS from the molds and we obtained a substrate with Gaussian bumps (Figure 6.3, top: step 3). Further details on the preparation method can be found in Section 6.2.2. Scanning electron microscopy (SEM) images of experimental Gaussian bumps and their molds are shown in Figure 6.3. Furthermore, we report in Figure A.4 in the Appendix some images of millimetre-size molds . While the mold has a resolution of 100 nm, which is defined by the printing accuracy, the PDMS structures present a smoother surface. We believe that the reason behind this is that the PDMS is an elastomer, and therefore it relaxes to the configuration which minimises its surface area.

It is known from literature that PDMS is *per se* hydrophobic and, when coated with lipids, it allows for the formation of a monolayer of lipids and not a bilayer[23]. To facilitate the formation of a bilayer, we hydrophilised the surface by cleaning it and treating it with UV/ozone. Details on the cleaning procedure are reported in Section 6.2.2.

Then, we positioned the PDMS microstructures in the flow chamber shown in Figure 6.1. We prepared a solution of small unilamellar vesicles (SUVs) from a mixture of lipids and flowed it into the chamber (Figure 6.3, bottom: step 1). After one hour of incubation, a lipid bilayer fully covers the PDMS substrate (Figure 6.3, bottom: step 2). From previous work on spherical SLBs imaged with transmission electron microscopy[20], we expect that the bilayer follows the curvature of the substrate with nanoscale precision.

In the bottom right of Figure 6.3, we show a schematic representation of the SLB. We use 5% mole ratio of the PEGylated lipid DOPE-PEG(2000) to increase the thickness of the water layer between the PDMS substrate and the lipid bilayer. While in our experiment this is useful to minimise the interaction between the surface of the support and the lipids, it can also be helpful for the incorporation of transmembrane proteins in the future. These proteins must be shielded from the surface of the solid substrate by using lipopolymers or polymer cushions[24].

Since we use micro-printing to design the molds, this method can be straightforwardly extended to arbitrary shapes. In Figure 6.4, we report examples of half-spherical,

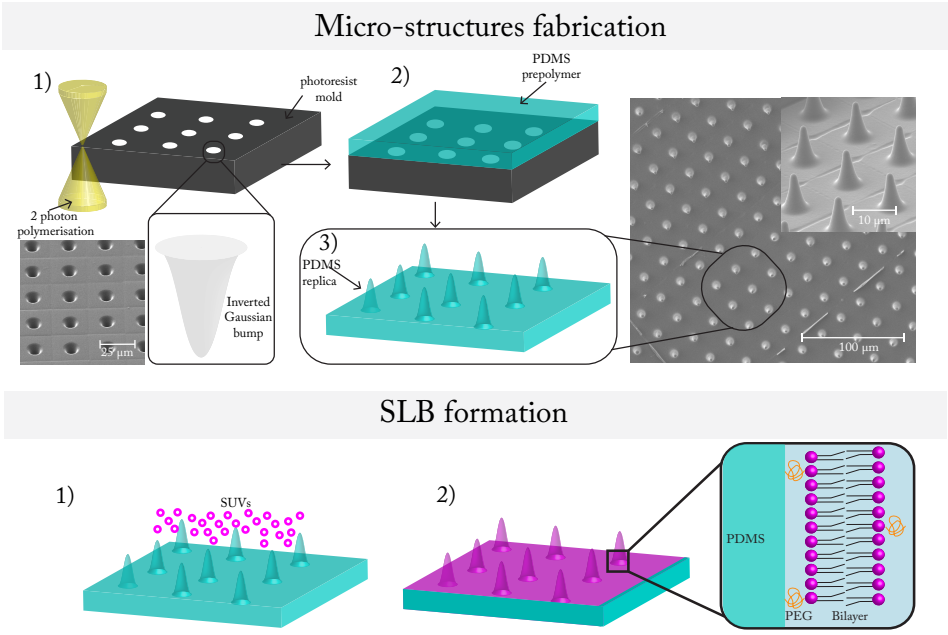

Figure 6.3: Overview of the experimental system. Microstructures fabrication. 1) Molds of Gaussian bumps are fabricated with two-photon polymerisation of a photo-resist. 2) PDMS pre-polymer is poured over the developed micro-printed molds and cured. 3) The resulting microstructures are peeled from the molds. Scanning electron microscopy (SEM) images of the PDMS Gaussian bumps and their mold counterparts are shown. **SLB formation.** 1-2) The microstructures are functionalised with a lipid bilayer by deposition of small unilamellar vesicles (SUVs). On the right, a close up view of the bilayer supported on the structures is shown. PEGylated lipids DOPE-PEG(2000) (orange) are used to increase the water layer between the PDMS substrate and the bilayer and therefore increase the fluidity of the bilayer (magenta).

toroidal, peanut-like, cylindrical microstructures, and their SLBs counterparts. We have chosen these shapes because they feature interesting combinations of mean and Gaussian curvature. As described in the introduction of this thesis, Section 1.2, these curvatures are commonly used to describe surfaces and they are equal to the average and the product of the principal curvatures, respectively.

Spheres are the simplest shape possible since their mean and Gaussian curvature are both constant and equal along the surface. The half-spheres in Figure 6.4a-e have positive varying curvatures and can be used to study the effect of the modulus of positive curvature on the membrane. The torii in Figure 6.4b-f have a continuous change from positive to negative Gaussian curvature from the outer to the inner side and can elucidate the effect of the sign of Gaussian curvature. The peanut-like structures in Figure 6.4c-g present a smooth saddle, which is relevant for studying different biological processes sensitive to

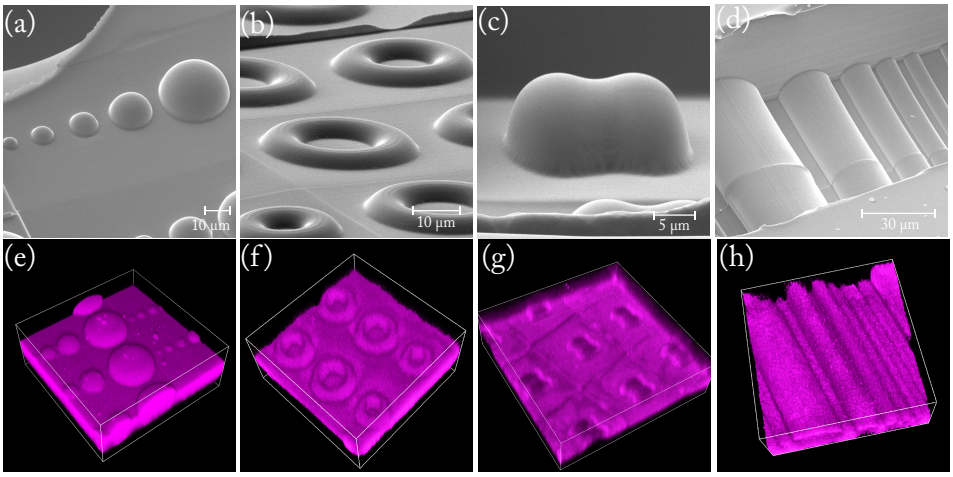

Figure 6.4: SLBs of designed shapes. SEM image of PDMS microstructures of **(a)** spherical, **(b)** toroidal, **(c)** peanut-like, and **(d)** cylindrical shape. 3D fluorescence volume reconstruction of the lipid bilayer on **(e)** spherical, **(f)** toroidal, **(g)** peanut-like, and **(h)** cylindrical shaped substrates.

negative Gaussian curvature. Finally, the cylinders in Figure 6.4 d-h feature zero Gaussian curvature. Therefore, they can be used to identify the consequences of different magnitudes of mean curvature.

6.3.2 Bilayer homogeneity and fluidity characterisation. For the SLB to be applicable in experiments of phase separation, protein localisation, diffusion, and more generally in applications in membrane mechanics, the bilayer has to be homogeneous and fluid. Homogeneity means that the bilayer uniformly covers the surface of the substrate and does not present defects. The homogeneity of the bilayer can be studied by fluorescence microscopy. If the bilayer is homogeneous, the lipids that are fluorescently labelled are homogeneously distributed on the surface, and, therefore, the fluorescent signal is on average constant over the sample. If substantial variations of the fluorescent signal can be observed, the bilayer is inhomogeneous. The fluidity of the bilayer can be measured by FRAP experiments. FRAP is a technique consisting of bleaching a part of the sample and measuring the recovery fluorescence signal[95;205]. By measuring how fast and to what extent the fluorescent signal recovers, the diffusion coefficient and the fraction of lipids able to diffuse on the surface can be estimated. A detailed description of the FRAP technique used in this chapter is presented in section 6.2.4.

To obtain a homogeneous and fluid bilayer on microstructures from 3D printing, we studied the bilayer properties on specific materials that allow for 3D printing. For comparison, we also measured them on glass, which is the most common material for lipid functionalisation[29]. We found that $\sim 100\%$ of the lipids are mobile on glass and that the diffusion coefficient is $\sim 4\,\mu m^2 s^{-1}$ (Table 6.1).

First, we tested commercially available resists for 3D printing, which allow fabricating

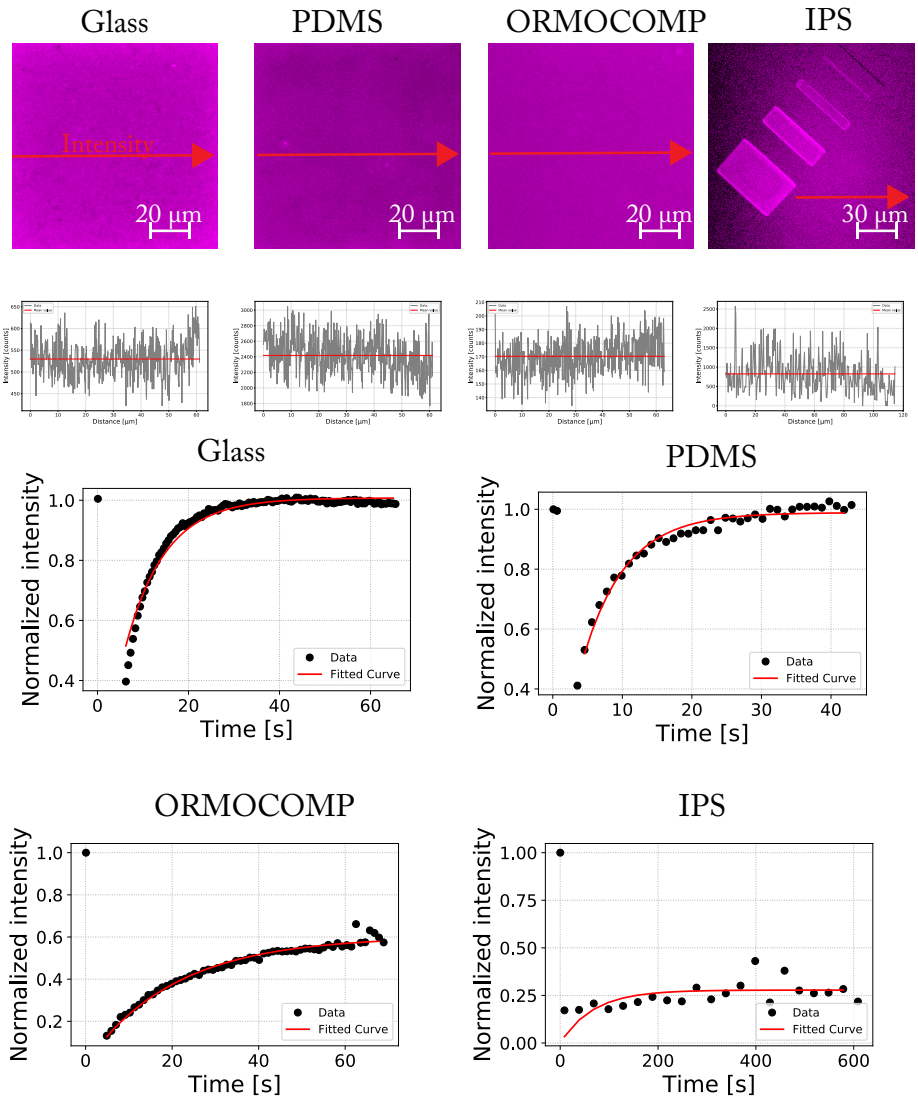

Figure 6.5: Top: bilayer homogeneity. Fluorescence images of the bilayer on glass, PDMS, ormocomp, and IPS. The intensity is measured along the red arrow and is plotted in grey under the images. **Bottom: bilayer fluidity.** FRAP on bilayers on the four materials. The fitting parameters are reported in Table 6.1.

Material	D_{FRAP} [$\mu m^2 s^{-1}$]	Fraction of mobile lipids [%]
Glass	4.08 ± 0.09	100.7755 ± 0.0008
PDMS	1.288 ± 0.001	98.886 ± 0.002
ORMOCOMP	0.4 ± 0.01	60.186 ± 0.004
IPS photoresist	0.2 ± 2.0	27.80 ± 0.04

Table 6.1: Measurements of the FRAP diffusion coefficient and the fraction of mobile lipids for different materials from fits of FRAP experiments. The FRAP data and curves are reported in Figure 6.5.

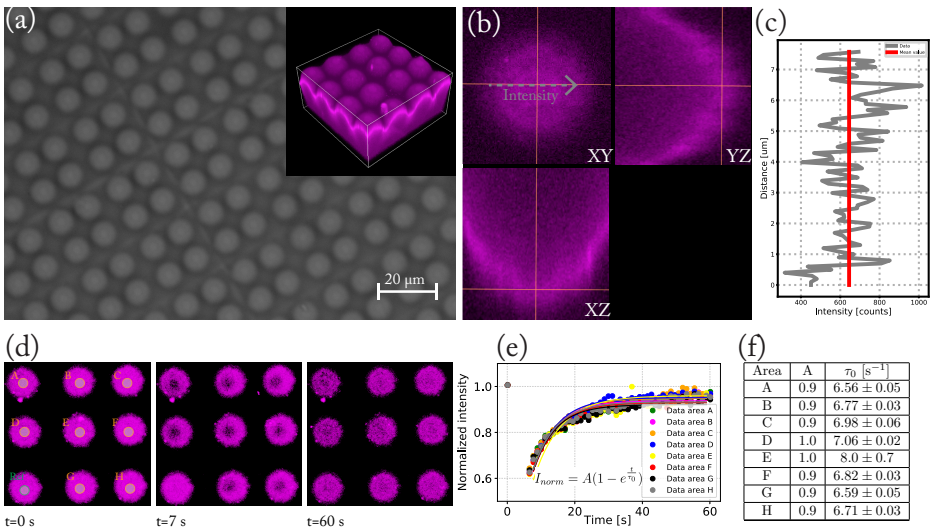

Area	A	τ_0 [s^{-1}]
A	0.9	6.56 ± 0.05
B	0.9	6.77 ± 0.03
C	0.9	6.98 ± 0.06
D	1.0	7.06 ± 0.02
E	1.0	8.0 ± 0.7
F	0.9	6.82 ± 0.03
G	0.9	6.59 ± 0.05
H	0.9	6.71 ± 0.03

Figure 6.6: Homogeneity and fluidity of the bilayer (a) Bright-field image of half-spherical microstructures. In the inset, we show a 3D reconstruction of the fluorescent lipid bilayer. **(b)** XY, YZ, and XZ projections of the bilayer on the top of the half-spheres. The intensity of the fluorescent signal along the grey axis is plotted in **(c)**. The intensity fluctuates around an average value, indicating that the bilayer is homogeneous. **(d)** FRAP experiments on 8 areas taken on the top of 8 half-spherical structures. The bleaching areas are labelled with letters from A to H and are shown in orange. The reference area is labelled in green. From left to right, the stages before, after bleaching, and at the end of the recovery are reported. **(e)** Experimental data and fits of the FRAP experiments. We can observe that the signal recovers almost to unity. The equation used in the fitting is reported in the inset. **(f)** Table of the experimental fitting parameters A and τ_0. The errors on A are of the order of $10^{-4} - 10^{-5}$. From the fits, it can be observed that the fluidity of the bilayer is consistent over the sample.

microstructures and direct lipid functionalisation. We used two polymer based photoresist: IPS photoresist and ORMOCOMP photoresist[206]. We chose the last one because it is made of a mixture of polymer and silicates, it is bio-compatible, and was previously employed in experiments with cells[207]. We coated the surfaces of both photoresists with lipids and observed that in both materials the bilayer was homogeneous (Figure 6.5). However, the fraction of lipids that were mobile was lower than on glass, namely $\sim$ 30% and $\sim$ 60% for IPS and ORMOCOMP, respectively (Table 6.1). This result can be ascribed to the presence of polymers, which affect lipid mobility, as also seen in Chapter 2 for polystyrene colloids. Moreover, for both materials, the diffusion coefficients measured by FRAP are one order of magnitude smaller than the one measured in glass. We attribute the increase in the fraction of mobile lipids and diffusivity in ORMOCOMP with respect to IPS to the presence of silicates in the chemical composition. Finally, we note that polymer-based photoresists, *e.g.* IPS, are often fluorescent over a broad spectrum of wavelengths, and, in this way, they interfere with the imaging of the bilayer in fluorescent microscopy.

Since the lipid bilayer was not fully mobile on these materials, we modified our method by first printing molds to be used for PDMS replica-molding. PDMS is known to be a suitable material for SLB formation[5;23]. We indeed observed that $\sim$ 100% of the lipids are mobile on PDMS and that the diffusion coefficient from FRAP experiments is of the same order of magnitude as the one on glass (Table 6.1).

To obtain a straightforward and comparable calculation of the bilayer fluidity, the measurements shown in Table 6.1 were performed on flat substrates. To show that the bilayer on PDMS maintains the homogeneity and the fluidity also on curved geometries, we tested a bilayer on a PDMS surface of half-spheres with a diameter of 8 μm. The half-spheres were obtained with the method illustrated in Figure 6.3. We show in Figure 6.6a a bright field image of the substrate and, in the inset, a fluorescence 3D reconstruction of the bilayer.

To test the homogeneity of the bilayer, we analysed the fluorescence intensity profile along one line taken on the top of one half-sphere (Figure 6.6b-c). We expect that if the intensity is constant, the bilayer is homogeneous and, if the intensity presents significant variations, the bilayer possess defects. From Figure 6.6c, we can observe that the value of the intensity randomly fluctuates around an average value, indicating that the bilayer is indeed homogeneous.

To test the fluidity of the bilayer, we performed FRAP experiments, and we reported the results in Figure 6.6d-f. We simultaneously bleached 8 circular areas taken on the top of 8 half-spherical microstructures (orange circle). We used as a reference a ninth area of the same size on the top of an unbleached half-sphere (green circle). For the bleaching and the reference areas, the same location on the half-spheres was used because the bleaching rate strongly depends on the height of the surface. We can observe from the time sequence of the FRAP experiment in Figure 6.6d that the fluorescent signal completely recovers. This can also be seen in Figure 6.6e, where the normalised intensity corrected for bleaching is plotted as a function of time. The signal in all the bumps recovers almost completely. The fluidity is consistent in the sample as all the recovery times except the one of region E

agree within error. The reason why the recovery in region E does not agree with the other ones is that small vesicles in the solution crossed the bleaching area during the experiment disturbing the measurements. Finally, we note that the different heights in the fitting curves can be attributed to the different bleaching rate over the sample, likely due to a tilt of the microscope stage. Moreover, we expect that complete recovery cannot be reached in this experiment because of the presence of PEGylated lipids that are bound to the surface. In our experiments, we used 5% of PEGylated lipids; therefore we anticipate that 5% of the lipids are stuck on the surface (for a schematic of the bilayer, see Figure 6.3).

6.3.3 FRAP measurements on non-planar bilayers. Theoretical and experimental studies have been performed to extend the calculation of the diffusion coefficient from FRAP measurements from planar to curved surfaces[208]. Brunger *et al.* in[209] made a comparison on FRAP experiment on planar and spherical surfaces. They showed that if a circular area on a plane and a half-sphere with the same surface area are bleached, the recovery does not depend on the surface geometry, but is sensitive to the difference in length of the boundary between the bleaching area and the surrounding. The latter result was later confirmed by Aizenbud *et al.*[210], who showed that the lipid exchange between the inside and outside of the bleaching area for cosine surfaces depends on the shape and the length of the boundary as well as the 3D geometry of the surface. More recently, Sbalzarini *et al.*[211] developed a computational method to simulate FRAP experiments on generic surfaces.

In this section, we demonstrate that the SLBs on microstructures introduced in the previous sections can be used as model systems for FRAP measurements in non-planar membranes. To study how membrane curvature affects FRAP measurements, half-spheres of varying radius were used as scaffolds for the membrane. These shapes were chosen because they have constant mean and Gaussian curvatures constant equal to $1/R$ and $1/R^2$ respectively, with R the sphere radius. The bleaching was performed on top of the half-spheres to simplify the estimation of the bleached area. Since the half-spheres have different heights and the bleaching rate is sensitive to the position on the half-spheres, no bleaching correction could be performed. Therefore the recovery cannot be complete even after long times. In Figure 6.7a, an example of a FRAP experiment performed on a half-sphere of radius equal to 3.5 µm is shown. For five different sphere radii, we measured the effective diffusion coefficient resulting from FRAP measurements (D_{FRAP}) with Equation 6.4. D_{FRAP} is plotted as a function of the sphere radius in Figure 6.7b. As the radius increases, D_{FRAP} decreases, which indicates that membrane geometry affects the recovery. In particular, we observe that the decay can be fitted with the following curve:

$$D_{FRAP} = A + \frac{B}{R^2} \tag{6.5}$$

with resulting fitting parameters A=(2.3 ± 0.1) µm^{2}s^{-1} and B=$(7.4 \pm 0.2$ µm^{4}s^{-1}). Beside our hypothesis, there are a lot of possible contributions from the experimental system to this result, *e.g.* the shape of the laser beam in the vicinity of surfaces of different curvatures.

We expect that these measurements can be extended to other shapes and that our method can shed some light on the effect of anisotropy in FRAP experiments. Finally,

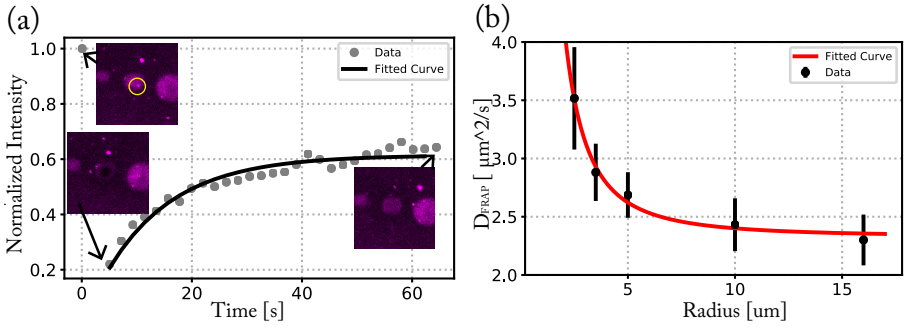

Figure 6.7: FRAP measurements of SLB on microstructures of half-spherical shape. (a) Fluorescence intensity as a function of time and exponential fit of the data. In the insets, a sequence of a FRAP experiment before bleaching, directly after bleaching, and after 64 s is shown. **(b)** FRAP effective diffusion coefficient as a function of the radius of the half-spheres.

we stress that the radius dependence of the effective diffusion coefficient calculated with FRAP does not represent a curvature dependence of the diffusion coefficient of the single lipids. The latter one, for the curvature differences relevant to this work, is independent on the underlying geometry.

6.3.4 Liquid-liquid phase separation on non-planar bilayers. For specific temperatures and lipid compositions, artificial lipid membranes undergo liquid-liquid phase separation into a more rigid, liquid-ordered (LO), and a softer, liquid-disordered (LD), phase. In this process, a correlation between the phase separation patterns and curvature has been observed in previous works. In this thesis, this correlation was studied by fixing the geometry of the membrane and analysing the phase separation patterns. Colloidal particles (Chapter 3) and substrates topographically patterned with colloidal particles (Chapter 5) were used as membrane scaffolds. While these systems allowed us to understand many aspects of this correlation, the limit in shape and size of colloidal particles prevented us to tune *a priori* the mean and Gaussian curvature finely. In this chapter, we show that microstructures made from 3D printing and replica-molding can be used to overcome this limitation and ultimately study the role of curvature on liquid-liquid phase separation.

To induce phase separation, the method described in Section 6.3.1 was modified in three ways: (1) The lipid mixture contained cholesterol, sphingomyelin, and POPC in mole ratio equal to 25:50:25. This lipid mixture was also used in Chapter 3 and 5, to obtain phase separation on colloidal particles and topographically patterned substrates. (2) The SUVs formation and lipid coating were performed at 70 °C to keep the lipids above the critical transition temperature during the bilayer formation. (3) After the lipid coating, the bilayer was cooled down from 70 °C to 25 °C at a cooling rate of 0.04 °Cmin^{-1}. This cooling rate allows for the lipids to arrange into microscopic domains on the PDMS surface. Experiments performed at higher cooling rates (*e.g.* 0.08 °Cmin^{-1}, the one used for MICA in Chapter 5 and by Goodchild *et al.* [195]) did not lead to micrometre scale phase

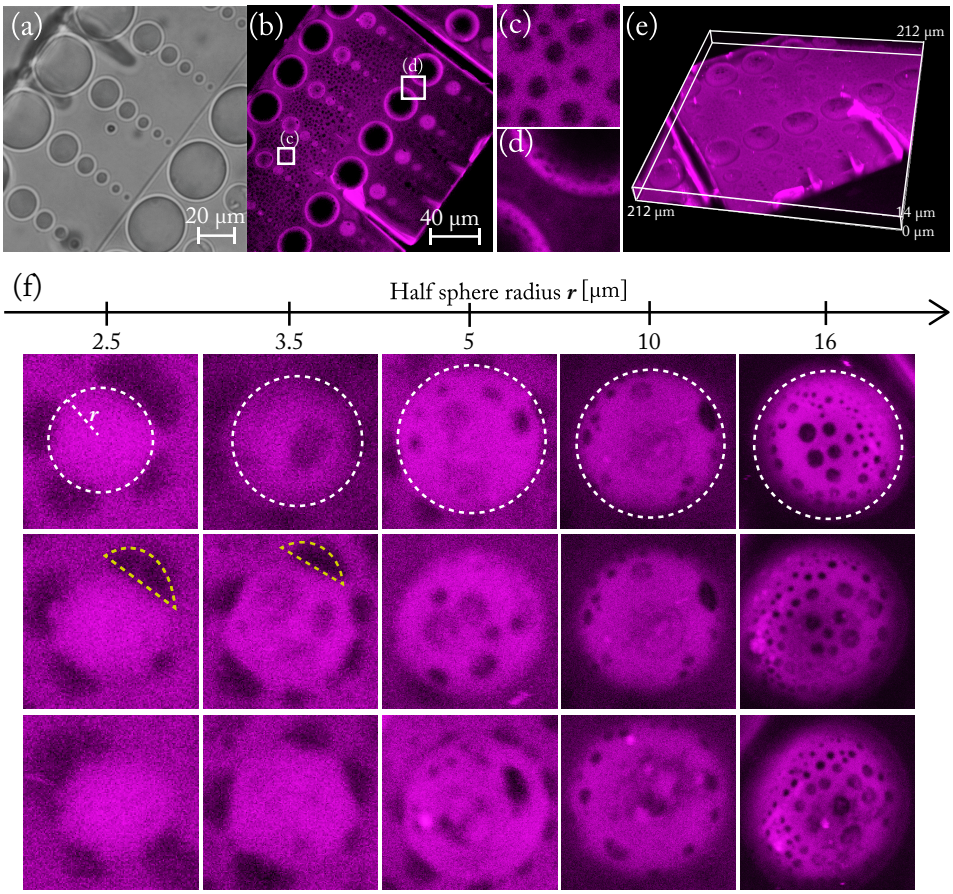

Figure 6.8: Phase-separated lipid bilayer on 3D microstructures. **(a)** Light microscopy image of half-spherical microstructures of varying radius. **(b)** Fluorescence microscopy image of a phase-separated lipid bilayer on half-spherical microstructures. The areas in the white squares are enlarged in **(c)** and **(d)**, where a flat area and the edges of two largest spheres are shown, respectively. **(e)** 3D reconstruction of the bilayer. **(f)** Top views of the phase-separated bilayer on three half-spheres of 2.5 µm, 3.5 µm, 5 µm, 10 µm and 16 µm radius. The LD phase is shown in magenta. The boundary of the half-spheres is shown by dotted white circles. As the radius increases, or the curvature decreases, the amount of LO domains on the half-spheres increases. This indicates a preference for the LO domains for the less curved regions. At the edge between the flat part and the half-spheres, the circular domain shape is affected by the half-spherical structures (dotted yellow lines).

separation on PDMS. We believe that lower cooling rates need to be used for PDMS than for MICA because the surface of PDMS is rougher than its MICA counterpart.

With these modifications, we observed liquid-liquid phase separation of the bilayer on half-spherical microstructures (see Figure 6.8). The half-spherical microstructures used have the same design of the ones employed for FRAP measurements in Section 6.3.3. A SEM image of the microstructures is shown in Figure 6.4 and a light microscopy image is reported in Figure 6.8a. First of all, we observe that the whole substrate is patterned with circular LO domains that are surrounded by the disordered phase, labelled in magenta. This can be seen from both the 2D view and the 3D reconstruction of the bilayer, reported in Figure 6.8b and e, respectively.

On the flat part of the substrate, of which a section is shown in Figure 6.8c, measurements on 50 domains showed that the average circular domain radius is $(0.9 \pm 0.3)\,\mu m$. The minimum and maximum domain radii measured are 0.3 µm and 1.6 µm, respectively. When the LO domains are in contact with the edge of the half-spherical microstructures, their shape deviates from a circle. This can be seen in Figure 6.8f, where top views of the half-spherical bilayer are reported. Three images for each radius of the half-spheres, whose value increases from left to right, are reported. In the dotted yellow circular segments, domains on the flat part close to the half-spheres are indicated and more of these domains can be recognised along the edge of the half-spheres. The edge between the flat substrate and the half-spheres is a region of high curvature and it may function as a barrier for the LO domains which change shape to comply to the edge of the microstructures.

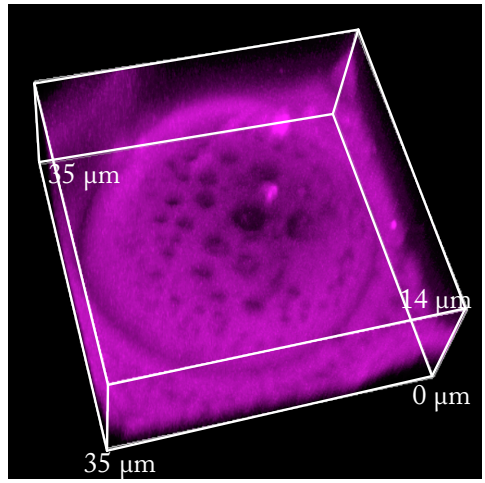

Figure 6.9: 3D reconstruction of the bilayer on an half-sphere. The top of this half-sphere is shown in Figure 6.8e on the top right. We can observe that the size of the LO domains increases from the bottom to the top.

The curvature also affects the occurrence of the LO domains on the half-spheres. On the half-spheres with smallest radius (r= 2.5 µm) and therefore highest curvature, no LO domains are observed, indicating that the curvature is high enough to pin the LD phase on the whole half-spherical surface. On less curved spheres (radius ranging from 3.5 µm to 16 µm), LO domains are present and appear circular. We can observe that the number of LO domains increases as the radius of the half-spheres increases. Moreover, the size of the LO domains increases with the radius of the half-sphere, indicating a preference for

the LO domains for the less curved regions, *i.e.* geometric pinning.

Finally, we note that on the largest half-spheres of 16 μm radius the size of the LO domains increases from the bottom to the top. This is clearly visible in a 3D reconstruction of the half-sphere of 16 μm radius on the top of Figure 6.8, shown in Figure 6.9. We believe that this effect may be due to the distance from the edge with the substrate. When the LO domains the further from the edge, they are less affected by the boundary, and, as a consequence, they can fuse more easily .

6.4 Conclusions

In conclusion, we have presented a simple method to fabricate supported lipid bilayers (SLBs) of designed curvature. The SLBs were made by lipid coating microstructures obtained by micro-printing and subsequent replica-molding with PDMS. We showed that microstructures of geometries with interesting curvatures, such as half-spheres, cylinders, torii, and peanut-like shapes can be obtained. Furthermore, we showed that the bilayer was homogeneous and fluid and we quantified the mobility with the fluorescence recovery after photobleaching (FRAP) technique.

We used these SLBs for FRAP measurements on anisotropic surfaces and we showed that the effective diffusion coefficient from FRAP experiments for half-spherical bilayers depends on the geometry of the micro-structures, and in particular the radius.

Furthermore, we employed these microstructures for liquid-liquid phase separation experiments. Interestingly, we found different phase separation patterns than in the experiments in Chapter 3 and 5. Specifically, we found that the bilayer was patterned with circular lipid domains. We showed that the curvature of the microstructures influences the distribution, the shape, and the size of these domains.

We expect that proteins, colloidal particles, and nanoparticles can be incorporated into the membrane to study single-particle diffusion on anisotropic surfaces. We anticipate that our set-up would be a perfect platform for studying localisation and dynamics of curvature sensing and generating proteins.

Finally, our method offers a very general way to obtain a thin liquid film confined on surfaces of designed curvature. On the more fundamental side, it can be used to study the many behaviours of two-dimensional liquids on curved geometries. On the more applied side, it offers a new way to obtain lubricating films which adhere to surfaces of nanoscale precision.

Acknowledgements

I thank Bas ten Haaf, Joseph Salaris, Casper van der Wel, and Ernst Jan Vegter for performing preliminary experiments. I am grateful to Jeroen Mesman, who fabricated the flow cell used in this chapter, Rachel Doherty for the electron microscopy imaging, and Piermarco Fonda for useful discussions.